Chin. Ann. Math. Ser. B
39(3), 2018, 535–552
DOI: 10.1007/s11401-018-0081-9

Chinese Annals of Mathematics, Series B

A DLM/FD/IB Method for Simulating Compound Cell Interacting with Red Blood Cells in a Microchannel*

Shihai ZHAO[1] Yao YU[2] Tsorng-Whay PAN[3] Roland GLOWINSKI[4]

(*Dedicated to Professor Philippe G. Ciarlet on the occasion of his* 80*th birthday*)

Abstract In this article, a computational model and related methodologies have been tested for simulating the motion of a malaria infected red blood cell (iRBC for short) in Poiseuille flow at low Reynolds numbers. Besides the deformability of the red blood cell membrane, the migration of a neutrally buoyant particle (used to model the malaria parasite inside the membrane) is another factor to determine the iRBC motion. Typically an iRBC oscillates in a Poiseuille flow due to the competition between these two factors. The interaction of an iRBC and several RBCs in a narrow channel shows that, at lower flow speed, the iRBC can be easily pushed toward the wall and stay there to block the channel. But, at higher flow speed, RBCs and iRBC stay in the central region of the channel since their migrations are dominated by the motion of the RBC membrane.

Keywords Compound cell, Red blood cells, Elastic spring model, Fictitious domain method, Immersed boundary method, Microchannel
2000 MR Subject Classification 76Z05, 76M10

1 Introduction

The biological cell is a lipid bilayer membrane encapsulating the cellular content. For eukaryotic cells, the influence of the internal structure on its dynamics in fluid flow is not yet fully understood. For example, the nucleus occupies 18% to 44% of the volume in human leukocytes (see [1]) and affects leukocyte adhesion to vascular endothelium. Another example is malaria infected RBCs (iRBCs for short) which have reduced deformability and shape changed and can disrupt the microcirculation of blood flow (see [2–3]). In general, vesicle and inextensible vesicle enclosing homogeneous fluid are often used to model the red blood cell (RBC for short). But to model those biological cells and to study the cell dynamics in fluid flow, a compound vesicle, which has a suspended rigid particle inside its membrane, immersed in a fluid was considered

Manuscript received October 31, 2017. Revised November 30, 2017.
[1]Department of Mathematics, Dongbei University of Finance and Economics, Dalian 116023, Liaoning, China. E-mail: shhzhao@dufe.edu.cn
[2]CGG, Houston, TX 77072, USA. E-mail: yuyaodouniao@gmail.com
[3]Department of Mathematics, University of Houston, Houston, TX 77204, USA. E-mail: pan@math.uh.edu
[4]Department of Mathematics, University of Houston, Houston, TX 77204, USA; Department of Mathematics, Hong Kong Baptist University, Hong Kong, China. E-mail: roland@math.uh.edu
*This work was supported by the National Science Foundation of the United States (Nos. DMS-0914788, DMS-1418308).

in [4]. The studies in [4] show that the internal structure does trigger the transition from tank-trading to tumbling in a two-dimensional bounded shear flow at Stokes regime in the absence of any viscosity mismatch. In [5], a bilamellar vesicle consisting of two vesicles has been used to study the influence of the internal structure of a biological cell (e.g., a leukocyte) on its dynamics and rheology: It was found that increasing the size of the inner vesicle (mimicking the nucleus) also triggers a tank-treading-to-tumbling transition in a two-dimensional bounded shear flow at Stokes regime. Concerning the dynamics of iRBCs in fluid flow, Plasmodium falciparum (P. falciparum for short) parasites inside the RBC membrane can be modeled as rigid particles (e.g., see [6]). Using a compound model (i.e., using a spring network for membrane and having a solid particle inside), the effect of iRBCs on the rheological property of blood in micro-channels has been investigated in [7]. In [8], simulations with a similar compound model successfully reproduce the experimental observation that how the iRBC transitions from passage to blockage in microfluidic channels.

In this article we have studied the motion of a compound vesicle and its interaction with RBCs in a Poiseuille flow by using a spring network to model the cell membrane and treating P. falciparum parasite inside cell membrane as a neutrally buoyant particle. In [9–11], computational methods combining such spring network model with an immersed boundary (IB for short) method for simulating the motion of RBCs in two-dimensional Poiseuille flows were developed. For simulating particle-fluid interaction, distributed Lagrange multiplier/fictitious domain (DLM/FD for short) formulations were developed and tested in, e.g., [12–15] for simulating the particle motion in fluid flow at finite Reynolds numbers. In the DLM/FD approach, the entire fluid-particle domain is considered to be a fluid. The fluid inside the particle boundary must exhibit a rigid-body motion. This constraint is enforced using a distributed Lagrange multiplier, which represents the additional body force per unit volume needed to maintain the rigid-body motion inside the particle, much like the pressure in incompressible fluid flow, whose gradient is the force required to maintain incompressibility. The integration of both DLM/FD method and IB method to simulate the interaction of neutrally buoyant particles and RBCs was first developed in [16]. Such combined method has been extended to simulate the dynamics of a compound vesicle (vesicle with a neutrally buoyant particle inside) and its interaction with RBCs in Poiseuille flows. Under the creeping flow condition, the motion of a compound vesicle in a Poiseuille flow was studied in [17]. Its migration is dominated by the motion of vesicle membrane. After migrating from the initial position next to the wall to the central region of the channel, the particle inside the membrane moves horizontally without crossing the streamlines as expected due to the lack of fluid inertia. When a compound vesicle interacts with several vesicles modeled as healthy RBCs in a microchannel under the creeping condition, they all migrate to the central region and stay there. But in this article, the fluid flow inertia has its effect on the compound vesicle at low Reynolds number. Besides the deformability of the red blood cell membrane, the migration of a neutrally buoyant particle inside the membrane is another factor to determine the iRBC motion. Typically an iRBC oscillates in a Poiseuille flow due to the competition between these two factors. Also the interaction of an iRBC and several RBCs shows that, at lower flow speed, the iRBC can be easily pushed toward the wall and stay there

to block the channel. But, at higher flow speed, RBCs and iRBC stay in the central region of the channel since their migrations are dominated by the motion of the RBC membrane. The content of the article is as follows. We discuss first our IB/DLM/FD formulation and then the related numerical schemes in Section 2. In Section 3, numerical results of a compound vesicle in Poiseuille flow are presented. The conclusions are summarized in Section 4.

2 Models and Methods

2.1 Fictitious domain formulation

Let Ω be a bounded rectangular domain filled with blood plasma which is incompressible, Newtonian, and contains RBCs and compound vesicles with the viscosity of the cytoplasm same as that of the blood plasma. We suppose, for simplicity, that Ω contains one compound vesicle (see Figure 1) in which there is a freely moving neutrally buoyant rigid disk $B(t)$ centered at $\mathbf{G}(t) = \{G_1, G_2\}^t$; the flow is modeled by the Navier-Stokes equations and the motion of the particle B is described by the Euler-Newton's equations. We define

$$W_{0,p} = \{\mathbf{v} \mid \mathbf{v} \in (H^1(\Omega))^2,\ \mathbf{v} = \mathbf{0} \text{ on } \Gamma \text{ and } \mathbf{v} \text{ is periodic in the } x_1 \text{ direction}\},$$
$$L_0^2 = \Big\{q \,\Big|\, q \in L^2(\Omega), \int_\Omega q\,\mathrm{d}\mathbf{x} = 0\Big\},$$
$$\Lambda_0(t) = \{\boldsymbol{\mu} \mid \boldsymbol{\mu} \in (H^1(B(t)))^2, \langle \boldsymbol{\mu}, \mathbf{e}_i\rangle_{B(t)} = 0,\ i = 1, 2,\ \langle \boldsymbol{\mu}, \overrightarrow{\mathbf{Gx}}^\perp\rangle_{B(t)} = 0\}$$

with Γ as the top and bottom of Ω, $\mathbf{e}_1 = \{1, 0\}^t$, $\mathbf{e}_2 = \{0, 1\}^t$, $\overrightarrow{\mathbf{Gx}}^\perp = \{-(x_2 - G_2), x_1 - G_1\}^t$ and $\langle\cdot,\cdot\rangle_{B(t)}$ an inner product on $\Lambda_0(t)$ which can be the standard inner product on $(H^1(B(t)))^2$ (see, e.g., [18], for further information on the choice of $\langle\cdot,\cdot\rangle_{B(t)}$). Then as in [12, 16], the fictitious domain formulation with distributed Lagrange multipliers for flow around a freely moving neutrally buoyant particle is as follows:

For a.e. $t > 0$, find $\mathbf{u}(t) \in (H^1(\Omega))^2$, $\mathbf{u}(t) = \mathbf{g}_0$ on Γ, $p(t) \in L_0^2$, $\mathbf{V}_\mathbf{G}(t) \in \mathbb{R}^2$, $\mathbf{G}(t) \in \mathbb{R}^2$, $\omega(t) \in \mathbb{R}$, $\boldsymbol{\lambda}(t) \in \Lambda_0(t)$ such that

$$\rho\int_\Omega \Big[\frac{\partial \mathbf{u}}{\partial t} + (\mathbf{u}\cdot\boldsymbol{\nabla})\mathbf{u}\Big]\cdot\mathbf{v}\ \mathrm{d}\mathbf{x} + 2\mu\int_\Omega \mathbf{D}(\mathbf{u}) : \mathbf{D}(\mathbf{v})\ \mathrm{d}\mathbf{x} - \int_\Omega p\boldsymbol{\nabla}\cdot\mathbf{v}\,\mathrm{d}\mathbf{x} - \langle\boldsymbol{\lambda}, \mathbf{v}\rangle_{B(t)}$$

$$= \rho\int_\Omega \mathbf{g}\cdot\mathbf{v}\,\mathrm{d}\mathbf{x} + \int_\Omega \mathbf{f}\cdot\mathbf{v}\,\mathrm{d}\mathbf{x}, \quad \forall\mathbf{v} \in W_{0,p}, \tag{2.1}$$

$$\int_\Omega q\boldsymbol{\nabla}\cdot\mathbf{u}(t)\mathrm{d}\mathbf{x} = 0, \quad \forall q \in L^2(\Omega), \tag{2.2}$$

$$\langle\boldsymbol{\mu}, \mathbf{u}(t)\rangle_{B(t)} = 0, \quad \forall\boldsymbol{\mu} \in \Lambda_0(t), \tag{2.3}$$

$$\frac{\mathrm{d}\mathbf{G}}{\mathrm{d}t} = \mathbf{V}_\mathbf{G}, \tag{2.4}$$

$$\mathbf{V}_\mathbf{G}(0) = \mathbf{V}_\mathbf{G}^0, \quad \omega(0) = \omega^0, \quad \mathbf{G}(0) = \mathbf{G}^0 = \{G_1^0, G_2^0\}^t, \tag{2.5}$$

$$\mathbf{u}(\mathbf{x}, 0) = \overline{\mathbf{u}}_0(\mathbf{x}) = \begin{cases}\mathbf{u}_0(\mathbf{x}), & \forall\mathbf{x} \in \Omega\backslash\overline{B(0)},\\ \mathbf{V}_\mathbf{G}^0 + \omega^0\{-(x_2 - G_2^0), x_1 - G_1^0\}^t, & \forall\mathbf{x} \in \overline{B(0)},\end{cases} \tag{2.6}$$

where $\mathbf{u}$ and p denote velocity and pressure, respectively, ρ is the fluid density, and μ is the fluid viscosity. We also assume that the flow field $\mathbf{u}$ is periodic in the x_1 direction with period

L, L being the length of the channel Ω, and the boundary condition is $\mathbf{g}_0 = \mathbf{0}$ for the Poiseuille flow and $\mathbf{g}_0 = (U, 0)^t$ (resp, $(-U, 0)^t$) on the top wall (resp., bottom wall) for the shear flow. In (2.1)–(2.6), we have $\mathbf{D}(\mathbf{v}) = \frac{\nabla \mathbf{v} + \nabla \mathbf{v}^t}{2}$, $\boldsymbol{\lambda}$ is a Lagrange multiplier, $\mathbf{g}$ is gravity, $\mathbf{f}$ is a body force which is the sum of $\mathbf{f}_p$ and $\mathbf{f}_B$ where $\mathbf{f}_p$ is the pressure gradient pointing in the x_1 direction and $\mathbf{f}_B$ accounts for the force acting on the fluid/cell interface (see the following sections), $\mathbf{V_G}$ is the translation velocity of the particle B, and ω is the angular velocity of the particle B. We suppose that the no-slip condition holds on ∂B. We also use, if necessary, the notation $\phi(t)$ for the function $\mathbf{x} \to \phi(\mathbf{x}, t)$.

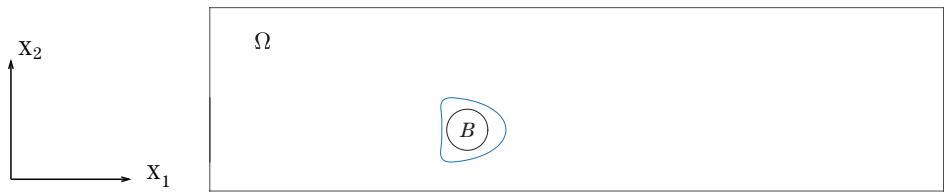

Figure 1 An example of computational domain with one compound vesicle.

Remark 2.1 The functional spaces we used in formula (2.1)–(2.6) are consistent with those employed in, e.g., [19], for $\mathbf{u}$ and $\partial \mathbf{u}/\partial t$, namely

$$\mathbf{u} \in L^\infty(0, T; H^1(\Omega))^2, \quad \frac{\partial \mathbf{u}}{\partial t} \in L^2((0, T) \times \Omega)^2$$

for all $T < T^*$ for some $T^* \in (0, \infty]$, where $\mathbf{u}$ is the global velocity field (fluid, particle and vesicle velocity field).

Remark 2.2 In (2.3), the rigid body motion in the region occupied by the particle is enforced via a Lagrange multiplier $\boldsymbol{\lambda}$. As discussed in [12], we solve the following equations to obtain the translation velocity $\mathbf{V_G}(t)$ and the angular velocity $\omega(t)$

$$\begin{cases} \langle \mathbf{e}_i, \mathbf{u}(t) - \mathbf{V_G}(t) - \omega(t)\, \overrightarrow{\mathbf{Gx}}^{\perp} \rangle_{B(t)} = 0 \quad \text{for } i = 1, 2, \\ \langle \overrightarrow{\mathbf{Gx}}^{\perp}, \mathbf{u}(t) - \mathbf{V_G}(t) - \omega(t)\, \overrightarrow{\mathbf{Gx}}^{\perp} \rangle_{B(t)} = 0. \end{cases} \tag{2.7}$$

Remark 2.3 In (2.1), $2\int_\Omega \mathbf{D}(\mathbf{u}) : \mathbf{D}(\mathbf{v})\, \mathrm{d}\mathbf{x}$ can be replaced by $\int_\Omega \nabla \mathbf{u} : \nabla \mathbf{v}\, \mathrm{d}\mathbf{x}$ since $\mathbf{u}$ is divergence free and in $W_{0,p}$. Also the gravity $\mathbf{g}$ in (2.1) can be absorbed into the pressure term.

Remark 2.4 A two-dimensional elastic spring network model used in [20] is considered in this paper to describe the deformable behavior of the RBCs. Based on this model, the RBC membrane can be viewed as made of membrane particles connecting with the neighboring membrane particles by springs, as shown in Figure 2. Elastic energy stores in the spring due to the change of the length l of the spring with respected to its reference length l_0 and the change in angle θ between two neighboring springs. The elastic energy of the RBC membrane, $E_m = E_l + E_b$, is the sum of the elastic energy for stretch/compression and the elastic energy for bending which are

$$E_l = \frac{k_l}{2} \sum_{i=1}^{N} \Big(\frac{l_i - l_0}{l_0} \Big)^2 \tag{2.8}$$

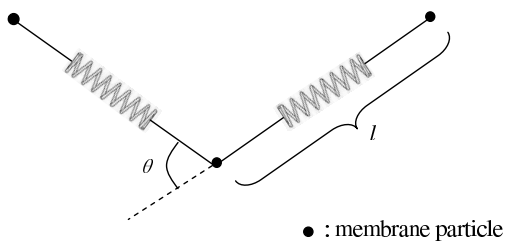

Figure 2 The elastic spring model of the RBC membrane.

and

$$E_b = \frac{k_b}{2}\sum_{i=1}^{N}\tan^2\Big(\frac{\theta_i}{2}\Big). \tag{2.9}$$

In (2.8)–(2.9), N is the total number of spring elements, and k_l and k_b are spring constants for changes in length and bending angle, respectively.

The process of creating the initial shape of RBCs can be found in [20]. The shape of the membrane is assumed to be a circle of radius $R_0 = 2.8$ μm initially. The circle is discretized into $N = 76$ membrane particles so that 76 springs of equal length are formed by connecting the neighboring particles. The shape change from a circle to the targeted one is caused by reducing the area of the circle through a penalty function

$$\Gamma_s = \frac{k_s}{2}\Big(\frac{s - s_e}{s_e}\Big)^2, \tag{2.10}$$

where s and s_e are the virtual area enclosed by the membrane and the targeted area of the RBC, respectively, and the total energy of the membrane is $E = E_m + \Gamma_s$. Based on the virtual work principle, the force acting on the ith membrane particle is now

$$\mathbf{F}_i = -\frac{\partial E}{\partial \mathbf{r}_i}, \tag{2.11}$$

where $\mathbf{r}_i$ is the position of the ith membrane particle. When the area is reduced, each membrane particle moves on the basis of the following equation of motion:

$$m\ddot{\mathbf{r}}_i + \gamma\dot{\mathbf{r}}_i = \mathbf{F}_i. \tag{2.12}$$

Here, $\dot{()}$ denotes the time derivative; m and γ represent the membrane particle mass and the membrane viscosity. The position $\mathbf{r}_i$ of the ith membrane particle is solved by discretizing (2.12) via a second order finite difference method. The total energy stored in the membrane decreases as the time elapses. The equilibrium shape of the RBC at rest is obtained as the total energy $E + \Gamma_s$ is minimized (see [21]). The reduced area of a RBC in this paper is defined by $s^* = \frac{s_e}{\pi R_0^2}$.

Remark 2.5 The immersed boundary method developed by Peskin (see, e.g, [22–24]) has been employed in this work because of its distinguish features in dealing with the problem of fluid flow interacting with a flexible fluid/structure interface. Over the years, it has demonstrated its capability to study computational fluid dynamics phenomena including blood flow. Based

on this method, the boundary of the deformable structure is discretized spatially into a set of boundary nodes. The force located at the immersed boundary node $\mathbf{X} = (X_1, X_2)$ affects the nearby fluid mesh nodes $\mathbf{x} = (x_1, x_2)$ through a 2D discrete δ-function $D_h(\mathbf{X} - \mathbf{x})$:

$$\mathbf{f}_B(\mathbf{x}) = \Sigma \mathbf{F}_i D_h(\mathbf{X}_i - \mathbf{x}) \quad \text{for } |\mathbf{X} - \mathbf{x}| \le 2h, \tag{2.13}$$

where h is the uniform finite element mesh size and

$$D_h(\mathbf{X} - \mathbf{x}) = \delta_h(X_1 - x_1)\delta_h(X_2 - x_2), \tag{2.14}$$

δ_h, the 1D discrete δ-functions, being defined by

$$\delta_h(z) = \begin{cases} \dfrac{1}{8h}\Big(3 - \dfrac{2|z|}{h} + \sqrt{1 + \dfrac{4|z|}{h} - 4\Big(\dfrac{|z|}{h}\Big)^2}\Big), & |z| \le h, \\ \dfrac{1}{8h}\Big(5 - \dfrac{2|z|}{h} - \sqrt{-7 + \dfrac{12|z|}{h} - 4\Big(\dfrac{|z|}{h}\Big)^2}\Big), & h \le |z| \le 2h, \\ 0, & \text{otherwise.} \end{cases} \tag{2.15}$$

The motion of the immersed boundary node $\mathbf{X}$ is also affected by the surrounding fluid and therefore is enforced by summing the velocities at the nearby fluid mesh nodes $\mathbf{x}$ weighted by the same discrete δ-function:

$$\mathbf{U}(\mathbf{X}) = \Sigma h^2 \mathbf{u}(\mathbf{x}) D_h(\mathbf{X} - \mathbf{x}) \quad \text{for } |\mathbf{X} - \mathbf{x}| \le 2h. \tag{2.16}$$

After each time step, the position of the immersed boundary node is explicitly updated by

$$\mathbf{X}_{t+\Delta t} = \mathbf{X}_t + \Delta t \mathbf{U}(\mathbf{X}_t). \tag{2.17}$$

2.2 Space approximation and time discretization

Concerning the finite element based space approximation of $\{\mathbf{u}, p\}$ in problem (2.1)–(2.6), we have used the P_1-iso-P_2 and P_1 finite element approximation (e.g., see [25] and [26, Chapter 5]). Let us consider the cell motion in a Poiseuille flow, i.e., $\mathbf{g}_0 = \mathbf{0}$ on Γ; a rectangular computational domain $\Omega \subset \mathbb{R}^2$ is chosen with length L and height H, h is a space discretization mesh size, $\mathcal{T}_h$ is a finite element triangulation of $\overline{\Omega}$ for velocity, $\mathcal{T}_{2h}$ is a twice coarser triangulation for pressure, and P_1 is the space of the polynomials in two variables of degree ≤ 1. The finite dimensional spaces are defined as

$$\begin{aligned} W_{0h} = \{&\mathbf{v}_h \mid \mathbf{v}_h \in C^0(\overline{\Omega})^2,\ \mathbf{v}_h|_T \in P_1 \times P_1,\ \forall T \in \mathcal{T}_h, \mathbf{v}_h = \mathbf{0} \text{ on } \Gamma \\ &\text{and is periodic in the } x_1 \text{ direction with period } L\}, \\ L_h^2 = \{&q_h \mid q_h \in C^0(\overline{\Omega}),\ q_h|_T \in P_1,\ \forall T \in \mathcal{T}_{2h},\ q_h \text{ is periodic in the } x_1 \\ &\text{direction with period } L\}. \end{aligned}$$

Now we define a finite dimensional space approximating $\Lambda_0(t)$ as follows: Choosing $\{\mathbf{x}_i\}_{i=1}^N$ as a set of points covering $\overline{B(t)}$; we define

$$\Lambda_h(t) = \Big\{\boldsymbol{\mu}_h \mid \boldsymbol{\mu}_h = \sum_{i=1}^N \boldsymbol{\mu}_i \delta(\mathbf{x} - \mathbf{x}_i),\ \boldsymbol{\mu}_i \in \mathbb{R}^2,\ \forall i = 1, \cdots, N\Big\}, \tag{2.18}$$

where $\delta(\cdot)$ is the Dirac measure at $\mathbf{x}=\mathbf{0}$. We then define $\langle\cdot,\cdot\rangle_{B_h(t)}$ by

$$\langle \boldsymbol{\mu}_h, \mathbf{v}_h\rangle_{B_h(t)} = \sum_{i=1}^{N} \boldsymbol{\mu}_i \cdot \mathbf{v}_h(\mathbf{x}_i), \quad \forall \boldsymbol{\mu}_h \in \Lambda_h(t),\ \mathbf{v}_h \in W_{0,h}. \tag{2.19}$$

The space $\Lambda_0(t)$ is defined by

$$\Lambda_{0,h}(t) = \{\mu_h \mid \mu_h \in \Lambda_h(t),\ \langle \mu_h, \mathbf{e}_i\rangle_{B_h(t)} = 0,\ i=1,2,\ \langle \mu_h, \overrightarrow{\mathbf{Gx}}^{\perp}\rangle_{B_h(t)} = 0\}. \tag{2.20}$$

A typical choice of points for defining $\Lambda_h(t)$ is to take the grid points of the velocity mesh internal to the region $B(t)$ and whose distance to the boundary of $B(t)$ is greater than, e.g. ch, for $0.5 \le c \le 1$ and to complete with selected points from the boundary of $B(t)$ whose distance to its neighboring boundary points is about kh for $1.5 \le k \le 2$ (e.g., see [27]).

Applying the Lie's scheme (see [26, 28]) to equations (2.1)–(2.6) with the backward Euler method in time for some subproblems, we obtain the following algorithm (some of the subscripts h have been dropped):

$\mathbf{u}^0 = \mathbf{u}_0$ is given; for $n \ge 0$, $\mathbf{u}^n$ being known, we compute the approximate solution via the following fractional steps:

(1) Solve

$$\begin{cases} \rho \displaystyle\int_\Omega \frac{\mathbf{u}^{n+\frac{1}{6}} - \mathbf{u}^n}{\triangle t} \cdot \mathbf{v} \mathrm{d}\mathbf{x} - \int_\Omega p^{n+\frac{1}{6}} (\boldsymbol{\nabla} \cdot \mathbf{v}) \mathrm{d}\mathbf{x} = 0, \quad \forall \mathbf{v} \in W_{0h}, \\ \displaystyle\int_\Omega q \boldsymbol{\nabla} \cdot \mathbf{u}^{n+\frac{1}{6}} \mathrm{d}\mathbf{x} = 0, \quad \forall q \in L_h^2, \\ \mathbf{u}^{n+\frac{1}{6}} \in W_{0,h}, \quad p^{n+\frac{1}{6}} \in L_h^2. \end{cases} \tag{2.21}$$

(2) Update the position of the membrane by (2.16)–(2.17) and then compute the force $\mathbf{f}_B^{n+\frac{1}{6}}$ on the fluid/cell interface by (2.11) and (2.13) and obtain $\mathbf{f}^{n+\frac{1}{6}} = \mathbf{f}_p + \mathbf{f}_B^{n+\frac{1}{6}}$.

(3) Solve

$$\begin{cases} \displaystyle\int_\Omega \frac{\partial \mathbf{u}(t)}{\partial t} \cdot \mathbf{v} \mathrm{d}\mathbf{x} + \int_\Omega (\mathbf{u}^{n+\frac{1}{6}} \cdot \boldsymbol{\nabla}) \mathbf{u}(t) \cdot \mathbf{v} \mathrm{d}\mathbf{x} = 0 \quad \text{on } (t^n, t^{n+1}),\ \forall \mathbf{v} \in W_{0h}, \\ \mathbf{u}(t^n) = \mathbf{u}^{n+\frac{1}{6}}, \\ \mathbf{u}(t) \in W_{0,h} \quad \text{on } (t^n, t^{n+1}), \end{cases} \tag{2.22}$$

and set $\mathbf{u}^{n+\frac{2}{6}} = \mathbf{u}(t^{n+1})$.

(4) Next, compute $\mathbf{u}^{n+\frac{3}{6}}$ via the solution of

$$\begin{cases} \rho \displaystyle\int_\Omega \frac{\mathbf{u}^{n+\frac{3}{6}} - \mathbf{u}^{n+\frac{2}{6}}}{\triangle t} \cdot \mathbf{v}\, \mathrm{d}\mathbf{x} + \mu \int_\Omega \boldsymbol{\nabla} \mathbf{u}^{n+\frac{3}{6}} : \boldsymbol{\nabla} \mathbf{v}\, \mathrm{d}\mathbf{x} = \int_\Omega \mathbf{f}^{\mathbf{n}+\frac{1}{6}} \cdot \mathbf{v}\, \mathrm{d}\mathbf{x}, \\ \forall \mathbf{v} \in W_{0,h}, \quad \mathbf{u}^{n+\frac{3}{6}} \in W_{0,h}. \end{cases} \tag{2.23}$$

(5) Now predict the position and the translation velocity of the center of mass of the particles as follows.

Take $\mathbf{V}_{\mathbf{G}}^{n+\frac{4}{6},0} = \mathbf{V}_{\mathbf{G}}^n$ and $\mathbf{G}^{n+\frac{4}{6},0} = \mathbf{G}^n$. Then predict the new position of the particle via the following sub-cycling and predicting-correcting technique:

For $k = 1, \cdots, N$, compute

$$\widehat{\mathbf{V}}_{\mathbf{G}}^{n+\frac{4}{6},k} = \mathbf{V}_{\mathbf{G}}^{n+\frac{4}{6},k-1} + \frac{\mathbf{F}^r(\mathbf{G}^{n+\frac{4}{6},k-1})\triangle t}{2N}, \tag{2.24}$$

$$\widehat{\mathbf{G}}^{n+\frac{4}{6},k} = \mathbf{G}^{n+\frac{4}{6},k-1} + \frac{(\widehat{\mathbf{V}}_{\mathbf{G}}^{n+\frac{4}{6},k} + \mathbf{V}_{\mathbf{G}}^{n+\frac{4}{6},k-1})\triangle t}{4N}, \tag{2.25}$$

$$\mathbf{V}_{\mathbf{G}}^{n+\frac{4}{6},k} = \mathbf{V}_{\mathbf{G}}^{n+\frac{4}{6},k-1} + \frac{(\mathbf{F}^r(\widehat{\mathbf{G}}^{n+\frac{4}{6},k}) + \mathbf{F}^r(\mathbf{G}^{n+\frac{4}{6},k-1}))\triangle t}{4N}, \tag{2.26}$$

$$\mathbf{G}^{n+\frac{4}{6},k} = \mathbf{G}^{n+\frac{4}{6},k-1} + \frac{(\mathbf{V}_{\mathbf{G}}^{n+\frac{4}{6},k} + \mathbf{V}_{\mathbf{G}}^{n+\frac{4}{6},k-1})\triangle t}{4N}, \tag{2.27}$$

enddo; and let

$$\mathbf{V}_{\mathbf{G}}^{n+\frac{4}{6}} = \mathbf{V}_{\mathbf{G}}^{n+\frac{4}{6},N}, \quad \mathbf{G}^{n+\frac{4}{6}} = \mathbf{G}^{n+\frac{4}{6},N}. \tag{2.28}$$

(6) Now, compute $\mathbf{u}^{n+\frac{5}{6}}$, $\boldsymbol{\lambda}^{n+\frac{5}{6}}$, $\mathbf{V}_{\mathbf{G}}^{n+\frac{5}{6}}$ and $\omega^{n+\frac{5}{6}}$ via the solution of

$$\begin{cases} \rho\displaystyle\int_\Omega \frac{\mathbf{u}^{n+\frac{5}{6}} - \mathbf{u}^{n+\frac{3}{6}}}{\triangle t}\cdot\mathbf{v}\,\mathrm{d}\mathbf{x} \ = \langle\boldsymbol{\lambda},\mathbf{v}\rangle_{B_h^{n+\frac{4}{6}}}, \quad \forall\mathbf{v}\in W_{0,h}, \\ \langle\boldsymbol{\mu},\mathbf{u}^{n+\frac{5}{6}}\rangle_{B_h^{n+\frac{4}{6}}} = 0, \quad \forall\boldsymbol{\mu}\in\Lambda_{0,h}^{n+\frac{4}{6}}, \\ \mathbf{u}^{n+\frac{5}{6}}\in W_{0,h}, \quad \boldsymbol{\lambda}^{n+\frac{5}{6}}\in\Lambda_{0,h}^{n+\frac{4}{6}}, \end{cases} \tag{2.29}$$

and solve for $\mathbf{V}_{\mathbf{G}}^{n+\frac{5}{6}}$ and $\omega^{n+\frac{5}{6}}$ from

$$\begin{cases} \langle\mathbf{e}_i, \mathbf{u}^{n+\frac{5}{6}} - \mathbf{V}_{\mathbf{G}}^{n+\frac{5}{6}} - \omega^{n+\frac{5}{6}}\overrightarrow{G^{n+\frac{4}{6}}x}^{\perp}\rangle_{B_h^{n+\frac{4}{6}}} = 0 \quad \text{for } i = 1,2, \\ \langle\overrightarrow{G^{n+\frac{4}{6}}x}^{\perp}, \mathbf{u}^{n+\frac{5}{6}} - \mathbf{V}_{\mathbf{G}}^{n+\frac{5}{6}} - \omega^{n+\frac{5}{6}}\overrightarrow{G^{n+\frac{4}{6}}x}^{\perp}\rangle_{B_h^{n+\frac{4}{6}}} = 0. \end{cases} \tag{2.30}$$

(7) Finally, take $\mathbf{V}_{\mathbf{G}}^{n+1,0} = \mathbf{V}_{\mathbf{G}}^{n+\frac{5}{6}}$ and $\mathbf{G}^{n+1,0} = \mathbf{G}^{n+\frac{4}{6}}$; and predict the final position and translation velocity as follows.

For $k = 1, \cdots, N$, compute

$$\widehat{\mathbf{V}}_{\mathbf{G}}^{n+1,k} = \mathbf{V}_{\mathbf{G}}^{n+1,k-1} + \frac{\mathbf{F}^r(\mathbf{G}^{n+1,k-1})\triangle t}{2N}, \tag{2.31}$$

$$\widehat{\mathbf{G}}^{n+1,k} = \mathbf{G}^{n+1,k-1} + \frac{(\widehat{\mathbf{V}}_{\mathbf{G}}^{n+1,k} + \mathbf{V}_{\mathbf{G}}^{n+1,k-1})\triangle t}{4N}, \tag{2.32}$$

$$\mathbf{V}_{\mathbf{G}}^{n+1,k} = \mathbf{V}_{\mathbf{G}}^{n+1,k-1} + \frac{(\mathbf{F}^r(\widehat{\mathbf{G}}^{n+1,k}) + \mathbf{F}^r(\mathbf{G}^{n+1,k-1}))\triangle t}{4N}, \tag{2.33}$$

$$\mathbf{G}^{n+1,k} = \mathbf{G}^{n+1,k-1} + \frac{(\mathbf{V}_{\mathbf{G}}^{n+1,k} + \mathbf{V}_{\mathbf{G}}^{n+1,k-1})\triangle t}{4N}, \tag{2.34}$$

enddo; and let

$$\mathbf{V}_{\mathbf{G}}^{n+1} = \mathbf{V}_{\mathbf{G}}^{n+1,N}, \quad \mathbf{G}^{n+1} = \mathbf{G}^{n+1,N},$$

and set

$$\mathbf{u}^{n+1} = \mathbf{u}^{n+\frac{5}{6}}, \quad \omega^{n+1} = \omega^{n+\frac{5}{6}}.$$

In the algorithm (2.21)–(2.34), we have $t^{n+\alpha} = (n+\alpha)\triangle t$, $\Lambda_{0,h}^{n+\alpha} = \Lambda_{0,h}(t^{n+\alpha})$, $B_h^{n+\alpha}$ is the region occupied by the particle centered at $\mathbf{G}^{n+\alpha}$, and $\mathbf{F}^r$ is a short range repulsion force which prevents the particle/cell penetration (see Remark 2.6).

The degenerated quasi-Stokes problem (2.21) is solved by a preconditioned conjugate gradient method (e.g., see [26]). The advection problem (2.22) for the velocity field is solved by a wave-like equation method as in [29] and [30], which is formally second-order accurate with respect to space and time discretizations. The associated CFL condition can be easily satisfied since the advection problem is decoupled from the rest, we can choose proper sub-time step here so that the above condition is satisfied. To enforce the rigid body motion inside the region occupied by the neutrally buoyant particles, we have applied the conjugate gradient method discussed in [12] to solve problem (2.29). Concerning predicting the particle translation velocity and position, there are two fractional steps resulted from the splitting of the Newton's equations, namely steps (5) and (7), in which we incorporate the repulsion force from the membrane with smaller sub-time step to prevents the particle/cell penetration. It would be simpler to have one step by combining steps (5) and (7), but we like to have the correction step right after the rigid body motion enforcement at the step (6).

Remark 2.6 When simulating the motion of a compound vesicle, we do need a repulsive force to prevent the overlapping between cell and particle. The repulsive force is obtained from the following Morse potential (e.g., see [31])

$$\phi(s) = k_r(1 - \mathrm{e}^{-(s-s_0)})^2,$$

where the parameter s is the shortest distance between the membrane particle and the surface of the solid particle and s_0 is the range of the repulsive force (when the distance s is greater than s_0, there is no repulsive force). The parameter k_r is a constant for the strength of the potential. At step (2) of algorithm (2.21)–(2.34), we then also compute $\mathbf{f}_r = -\frac{\partial \phi(s)}{\partial s}$ for each membrane particle which is close to a solid particle. Also the force acting on the particle from all membrane points can be obtained and denoted by $\mathbf{F}^r$. Similarly the repulsive force similar to the one given above can be used to prevent the overlapping of vesicles which might occur in simulations.

Remark 2.7 In [21], we have validated the immersed boundary method with the elastic spring model by comparing the numerical results with previous experimental data (see [32]), theoretical Keller and Skalak model (see [33]), and simulations [34, 35] for the inclination angles and tank-treading frequencies of single RBC in shear flow. Also the distributed Lagrange multiplier/fictitious domain (DLM/FD for short) formulation for simulating neutrally buoyant particle motion was developed and tested in [12].

3 Numerical Results and Discussions

The initial shapes of the cells used in this article for the flow simulations are obtained via the procedure described in [20–21] and Remark 2.4. For modelling the cells, we have chosen the same

parameter values used in [20], namely, the bending constant in (2.9) is $k_b = 5\times10^{-10}$ N · m, the spring constant in (2.8) is $k_l = 5\times10^{-8}$ N · m, the penalty coefficient in (2.10) is $k_s = 10^{-5}$ N · m. The parameter for the repulsive force is $k_r = 5\times10^{-8}$ N · m. The cells are suspended in a blood plasma which has a density $\rho = 1.00$ g/cm^3. The viscosity ratio which describes the viscosity contrast of the fluid inside and outside the RBC membrane is fixed at 1.0. The computational domain is a two dimensional horizontal channel. In the simulation, a constant pressure gradient is prescribed as a body force. In addition, periodic conditions are imposed at the left and right boundary of the domain. The Reynolds number is defined by $\mathrm{Re} = \frac{\rho U H}{\mu}$ where U is the velocity at the central line in the channel when containing no cells and H is the height of the channel. Since a malaria-infected RBC (iRBC for short) undergoes a series of changes at different stages, the parasite forms a round ring shape in the early stage and keeps growing in size. At late stages the parasite forms a core inside the cell, causing the cell to lose its biconcave shape and turn into an elliptical shape. Thus the shape of iRBC considered in this section is close to an elliptical shape and the filling fraction of the particle varies from 0.05 to 0.4.

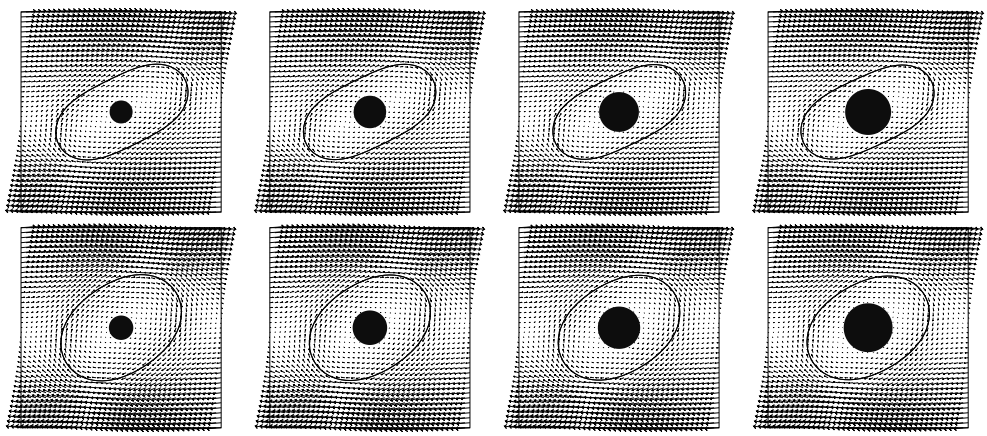

Figure 3 Position of a compound cell and velocity field next to the cell at the steady tank-treading state of a compound iRBC in a shear flow: The cell swelling ratios is s^*=0.84 for the upper row and 0.95 for the lower row. The filling fraction is ϕ = 0.05, 0.1, 0.15 and 0.2 from left to right for each row.

3.1 A compound cell in a shear flow

In this subsection, we perform a series of numerical tests to simulate the motions of a compounded iRBC in a shear flow. The computational domain is 20×20 μm^2 as in [36]. The shear rate of the flow is set as 50 s^{-1}. The fluid viscosity is $\nu = 0.12$ g/(cm s). Two different swelling ratios ($s^* = 0.84$ and 0.95) of cells are used. The filling fraction $\phi = a^2\pi/s^*$ of the particle varies from 0.05 to 0.2 where a is the radius of the disk inside the cell. The particle mass center of the compounded iRBC is fixed at center of the domain $(10, 10)$ as considered in [36]. The grid resolution for the computational domain is 80 grid points per 10 μm. The time

step is 0.00001 ms. As the filling fraction increases, the angle between the cell long axis and the horizontal line decreases as shown in Figures 3–4. This can be explained as follows: By including a solid particle, the energy dissipation increases, so the compound interface behaves like an inclusion-free interface that encapsulates a more viscous fluid. The larger the inclusion is, the higher the effective viscosity will be. And as shown in Figure 4, the steady inclination angle is close to the one reported in [36].

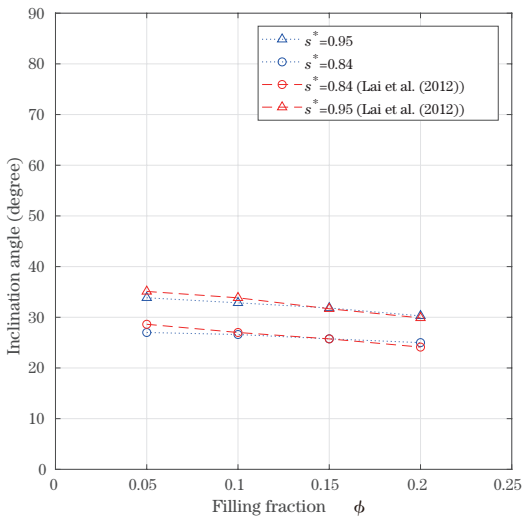

Figure 4 Plot of steady inclination angle as a function of filling fraction.

3.2 Migration of a compound cell in a Poiseuille flow

To use the above methodology to simulate the motion of a compound vesicle in a Poiseuille flow, we have assumed first that the domain of computation is $\Omega = 80 \times 10\ \mu\text{m}^2$. The compound cell swelling ratio is $s^* = 0.9$ and its filling fractions $\phi = \pi a^2/s_e$ are 0.2, 0.3, and 0.4. The fluid viscosity is $\nu = 0.012$ g/(cm s). For driving the Poiseuille flow, we have applied a pressure gradient as a force in the horizontal direction so that the maximum speed at the central line is 0.1 (resp., 0.5, and 1) cm/s when having no compound vesicle and the Reynolds number is Re = 0.008333 (resp., 0.04166 and 0.08333). The initial velocity is zero everywhere. The grid resolution for the computational domain is 80 grid points per 10 μm. The time step is 0.00001 ms.

The compound vesicle is placed next to the bottom wall with the particle mass center 3 μm above the wall, the inclination angle being zero (see Figure 5). If we consider only a deformable vesicle placed at the same initial position, the vesicle migrates toward the central region of the channel. If a rigid particle is placed at the initial position, due to the shear gradient of Poiseuille flow and the wall effect, the particle will travel to an equilibrium position somewhere in between the channel central axis and the wall, which is known as the Segré-Silberberg effect (see [37]). The equilibrium position depends on the Reynolds number (see, e.g, [12]). Now

we have a rigid particle inside a deformable membrane as a compound vesicle. The lateral migration of the compound vesicle is determined by the combined effect of the trends from the deformable membrane and the particle. When the particle inside the vesicle is small, the force on the particle is weak compared to the force on the deformable membrane. The deformable membrane is dominating and the compound vesicle is migrating toward the central of the channel. When the particle inside the vesicle is larger, the force on the particle is on par with the force on the deformable membrane. The particle itself may rest at its equilibrium position, while the force on the membrane make the compound vesicle migrate toward the central of the channel. Due to inertia, if the compound vesicle makes its way across the central axis of the channel, the force on the particle will drive it to its symmetric equilibrium position. The compound vesicle will also migrate toward the symmetric equilibrium position of the particle since the force on the membrane drives it back to the central axis is weak due to the fact that the displacement from the central is tiny. Thus the compound vesicle oscillates between the two equilibrium positions of the particle. The positions of the particle and membrane at different times are shown in Figure 5 for $\phi = 0.2,\ 0.3$, and 0.4. The histories of the mass center of the neutrally buoyant particle for different filling fractions and maximum speeds are presented in Figure 6. But for lower maximum speeds $U = 0.1$ and 0.5 cm/s, the effect of deformability from the membrane is weaker so that the compound cell oscillates slowly.

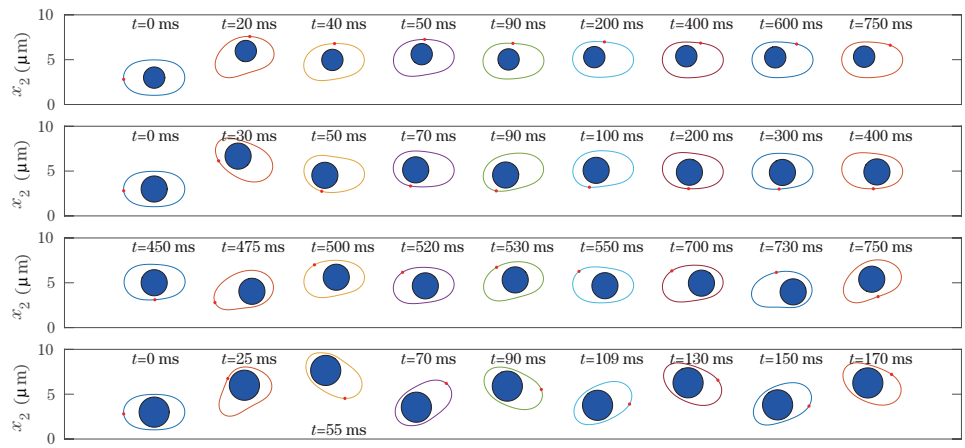

Figure 5 Particle and membrane positions: $\phi = 0.2$ (top), 0.3 (middle two), and 0.4 (bottom).

3.3 Interaction of a compound cell and RBCs in a Poiseuille flow

The interaction between healthy RBCs and iRBC in a narrow channel is investigated in this subsection. The computational domain is set as $40 \times 10\ \mu m^2$. The parameters for the RBC and fluid properties are the same as in the previous section. For the iRBC, the cell swelling ratio is $s^* = 0.9$ and the filling fraction is $\phi = 0.4$. The healthy red blood cell has a biconcave shape with swelling ratio of 0.481. The maximum velocity on the channel central axis without cells

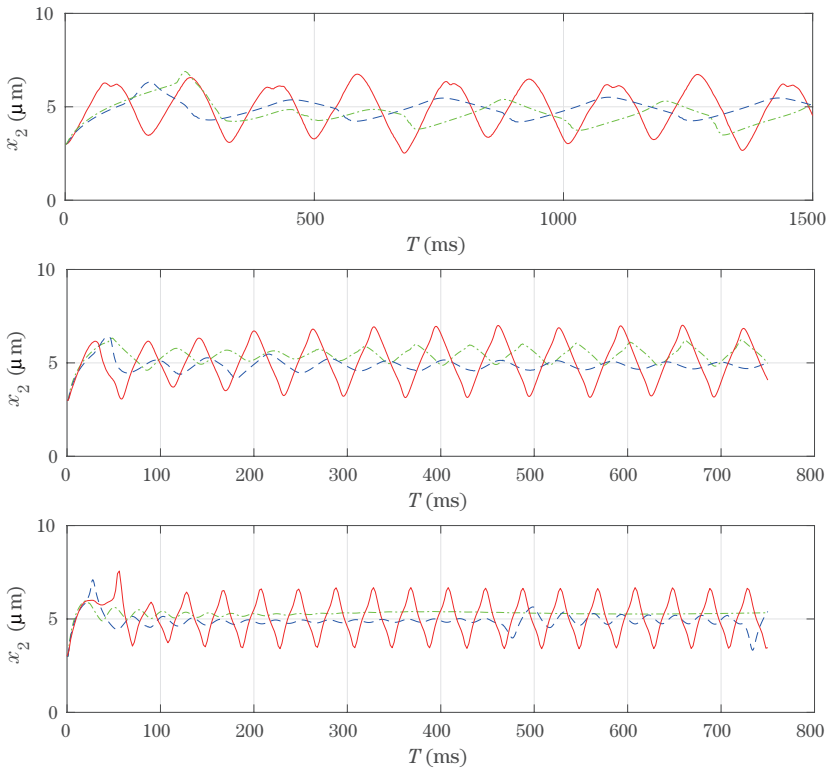

Figure 6 Histories of the mass center of the neutrally buoyant particle inside a vesicle for $\phi = 0.2$ (green dashed-dotted line), 0.3 (blue dashed line), and 0.4 (red solid line). The maximum speeds are $U = 0.1,\ 0.5$ and 1 (from top to bottom).

is 0.1 cm/s. Then the interaction between 5 healthy RBCs and an iRBC is investigated. The 6 cells are distributed in the domain with even spacing and initial inclination angles of zero degree. Once the cells start to move, the iRBC moves toward the central region faster due to the combined lifting force from the membrane and particle. Those RBCs also migrate toward the central region later on. After RBCs catch up with the iRBC, they usually remain in the central region of the channel. But due to the presence of an oscillating iRBC in the channel, they tend to pass by the iRBC through the space between the iRBC and the channel wall when iRBC is closer to the wall. This passing through of RBCs pushes the iRBC further to the side of the channel and creates a blockage inside the channel. An illustration of the procedure of a RBC bypassing an iRBC is shown in Figures 7–8. In Figure 9, the trajectory of cell mass center is plotted. The blue solid line represents the trajectory of iRBC while the red dashed lines represent the RBCs. The fact that the red dashed line is above the blue solid lines means that the iRBC is pushed toward the lower channel wall by the healthy RBCs. Because the cells are stacked up, keeping in mind that the inclusion in the iRBC has a radius of about 1.7 μm and it is pushed against the wall most of the time later on. But for a faster flow speed at the channel center, $U = 1$ cm/s, RBCs and iRBC all tend to stay away from both walls as shown

in Figure 9 since their migrations are dominated by the motion of the RBC membrane.

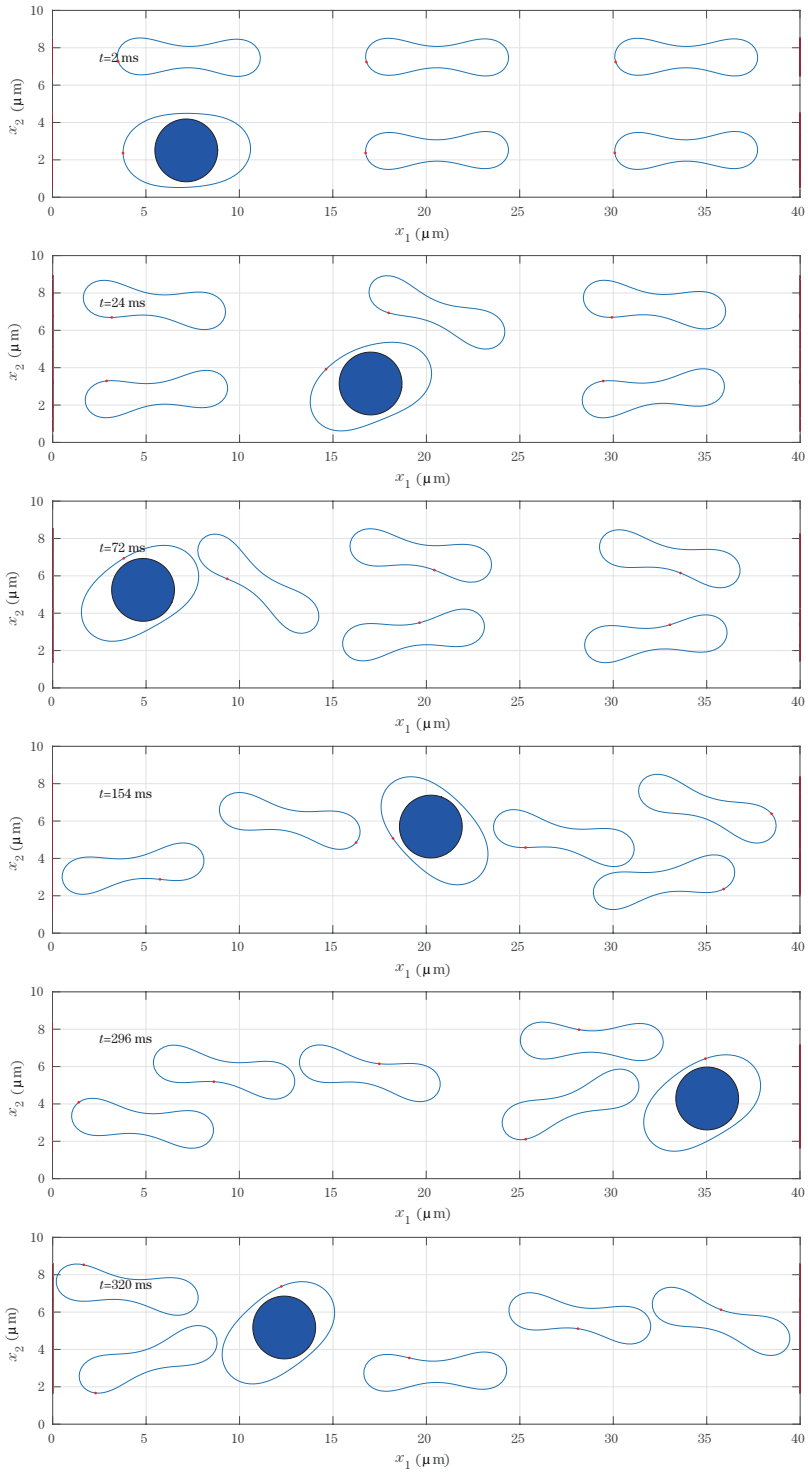

Figure 7 Positions of the RBCs: $t = 2,\ 24,\ 72,\ 154, 296$ and 320 ms (from top to bottom).

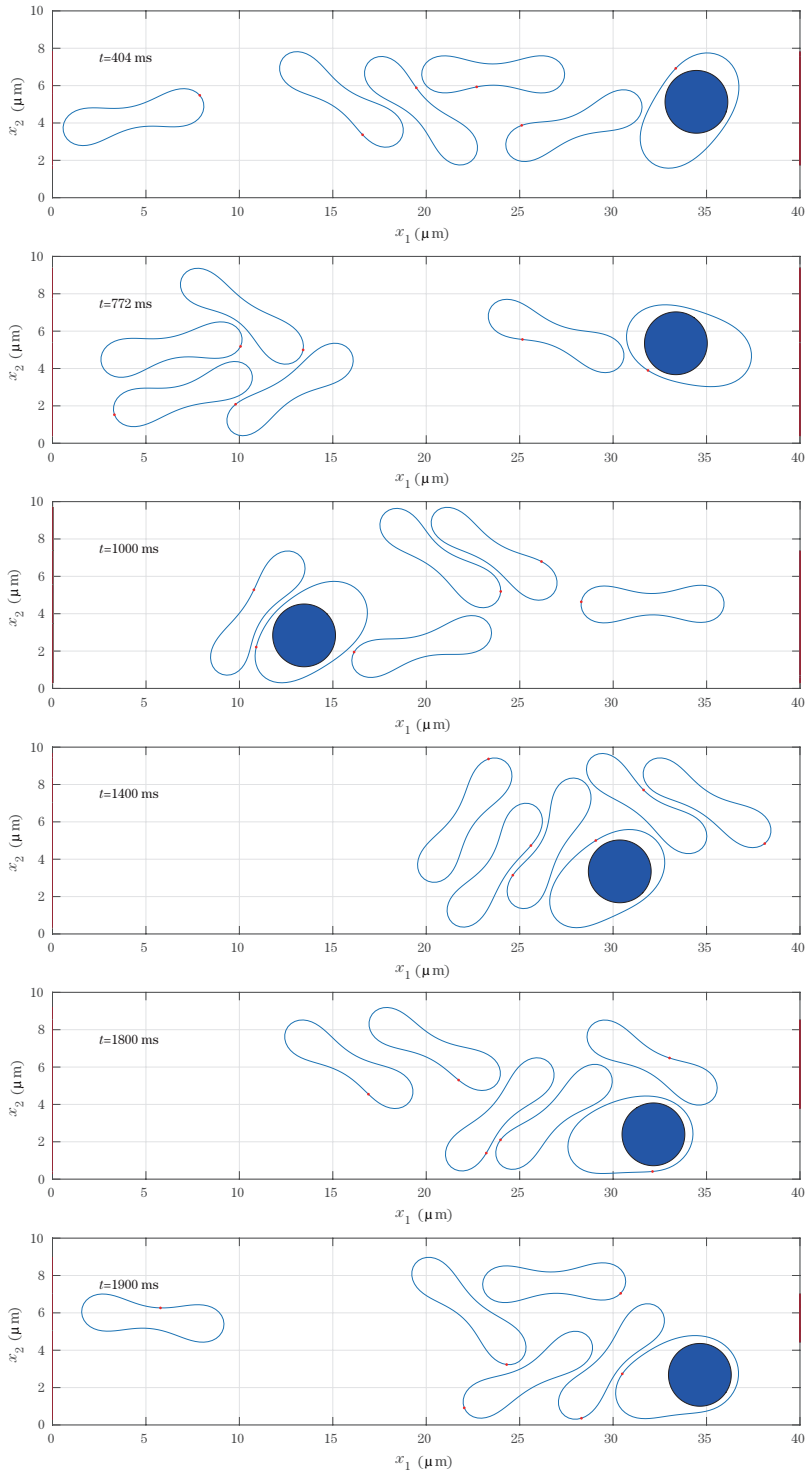

Figure 8 Positions of the RBCs: $t = 404,\ 772,\ 1000,\ 1400,\ 1800$ and 1900 ms (from top to bottom).

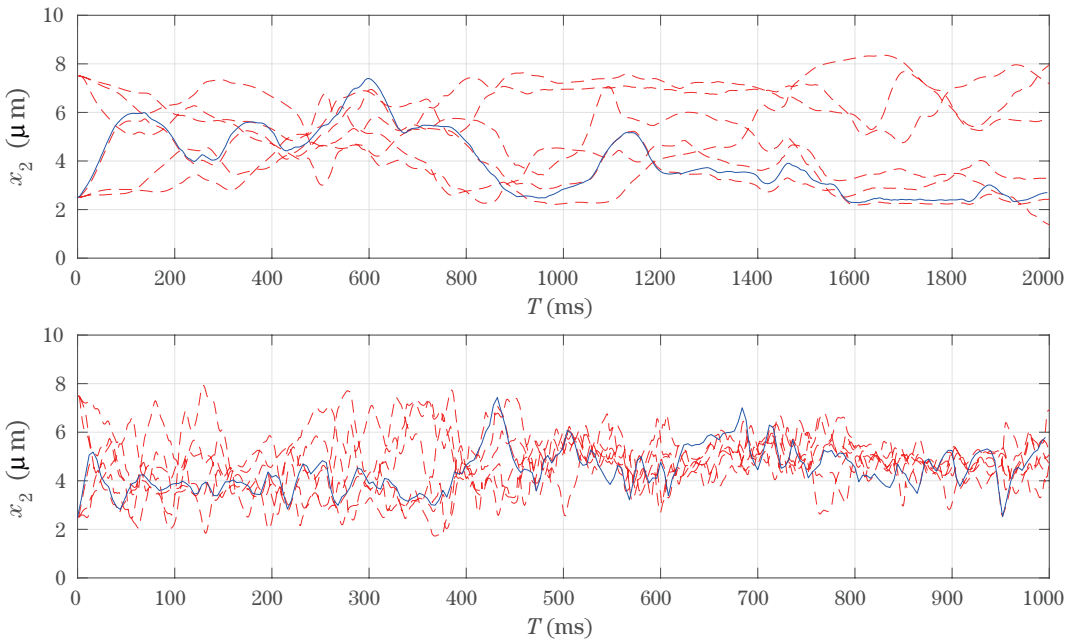

Figure 9 Histories of the height of the mass centers of RBCs (dashed lines) and particle (solid line): $U = 0.1$ cm/s (top) and 1 cm/s (bottom).

4 Conclusions

In summary, a computational model and related numerical methodologies have been tested for simulating the motion of an iRBC in Poiseuille flow. The motion of a compound vesicle at low Reynolds number was studied. Besides the deformability of the membrane, the migration of neutrally buoyant particle is another factor to determine the motion of a compound vesicle in Poiseuille flow. The iRBC oscillates inside a channel. The oscillating frequency depends on the flow speed and its oscillating amplitude depends on the solid fraction. The interaction of an iRBC and several RBCs shows that, at lower flow speed, the iRBC is easy to be pushed closer to the wall and stay there to block the channel. But, at higher speed, RBCs and iRBC stay in the central region of the channel. The numerical results in this paper are qualitatively similar to experimental observations and other investigators' findings (see [7]) and thus show the potential of this numerical method for future studies of blood flow in microcirculation and microchannels in three dimensions.

References

[1] Schmid-Schonbein, G. W., Shih, Y. Y. and Chien, S., Morphometry of human leukocytes, *Blood*, **56**, 1980, 866–875.

[2] Diez-Silva, M., Dao, M., Han, J., et al., Shape and biomechanical characteristics of human red blood cells in health and disease, *MRS Bull.*, **35**, 2010, 382–388.

[3] Glenister, F. K., Coppel, R. L., Cowman, A. F., et al., Contribution of parasite proteins to altered mechanical properties of malaria-infected red blood cells, *Blood*, **99**, 2002, 1060–1063.

[4] Veerapaneni, S. K., Young, Y.-N., Vlahovska, P. M. and Blawzdziewicz, J., Dynamics of a compound vesicle in shear flow, *Phys. Rev. Lett.*, **106**, 2011, 158103.

[5] Kaoui, B., Krüger, T. and Harting, J., Complex dynamics of a bilamellar vesicle as a simple model for leukocytes, *Soft Matter*, **9**, 2013, 8057–8061.

[6] Nash, G. B., O'Brien, E., Gordon-Smith, E. C. and Dormandy, J. A., Abnormalities in the mechanical properties of red blood cells caused by Plasmodium falciparum, *Blood*, **74**, 1989, 855–861.

[7] Imai, Y., Kondo, H., Ishikawa, T., et al., Modeling of hemodynamics arising from malaria infection, *J. Biomech.*, **43**, 2010, 1386–1393.

[8] Wu, T. and Feng, J. J., Simulation of malaria-infected red blood cells in microfluidic channels: Passage and blockage, *Biomicrofluidics*, **7**, 2013, 044115.

[9] Shi, L., Pan, T.-W. and Glowinski, R., Deformation of a single blood cell in bounded Poiseuille flows, *Phys. Rev. E*, **85**, 2012, 016307.

[10] Shi, L., Pan, T.-W. and Glowinski, R., Lateral migration and equilibrium shape and position of a single red blood cell in bounded Poiseuille flows, *Phys. Rev. E*, **86**, 2012, 056308.

[11] Shi, L., Pan, T.-W. and Glowinski, R., Numerical simulation of lateral migration of red blood cells in Poiseuille flows, *Int. J. Numer. Methods Fluids*, **68**, 2012, 1393–1408.

[12] Pan, T.-W. and Glowinski, R., Direct simulation of the motion of neutrally buoyant circular cylinders in plane Poiseuille flow, *J. Comput. Phys.*, **181**, 2002, 260–279.

[13] Pan, T.-W. and Glowinski, R., Direct simulation of the motion of neutrally buoyant balls in a three-dimensional Poiseuille flow, *C. R. Mecanique, Acad. Sci. Paris*, **333**, 2005, 884–895.

[14] Pan, T.-W., Chang, C.-C. and Glowinski, R., On the motion of a neutrally buoyant ellipsoid in a three-dimensional Poiseuille flow, *Comput. Methods Appl. Mech. Engrg.*, **197**, 2008, 2198–2209.

[15] Pan, T.-W., Huang, S.-L., Chen, S.-D., et al., A numerical study of the motion of a neutrally buoyant cylinder in two dimensional shear flow, *Computers & Fluids*, **87**, 2013, 57–66.

[16] Pan, T.-W., Shi, L. and Glowinski, R., A DLM/FD/IB method for simulating cell/cell and cell/particle interaction in microchannels, *Chinese Annals of Mathematics, Series B*, **31**, 2010, 975–990.

[17] Pan, T.-W., Zhao, S., Niu, X. and Glowinski, R., A DLM/FD/IB method for simulating compound vesicle motion under creeping flow condition, *J. Comput. Phys.*, **300**, 2015, 241–253.

[18] Glowinski, R., Pan, T. W., Hesla, T., et al., A fictitious domain approach to the direct numerical simulation of incompressible viscous flow past moving rigid bodies: Application to particulate flow, *J. Comput. Phys.*, **169**, 2001, 363–427.

[19] Desjardins, B. and Esteban, M. J., Existence of weak solutions for the motion of rigid bodies in a viscous fluid, *Arch. Rational Mech. Anal.*, **146**, 1999, 59–71,

[20] Tsubota, K., Wada, S. and Yamaguchi, T., Simulation study on effects of hematocrit on blood flow properties using particle method, *J. Biomech. Sci. Eng.*, **1**, 2006, 159–170.

[21] Wang, T., Pan, T. W., Xing, Z. and Glowinski, R., Numerical simulation of rheology of red blood cell rouleaux in microchannels, *Phys. Rev. E*, **79**, 2009, 041916.

[22] Peskin, C. S., Numerical analysis of blood flow in the heart, *J. Comput. Phys.*, **25**, 1977, 220–252.

[23] Peskin, C. S. and McQueen, D. M., Modeling prosthetic heart valves for numerical analysis of blood flow in the heart, *J. Comput. Phys.*, **37**, 1980, 11332.

[24] Peskin, C. S., The immersed boundary method, *Acta Numer.*, **11**, 2002, 479–517.

[25] Bristeau, M. O., Glowinski, R. and Périaux, J., Numerical methods for the Navier-Stokes equations, applications to the simulation of compressible and incompressible viscous flow, *Computer Physics Reports*, **6**, 1987, 73–187.

[26] Glowinski, R., Finite element methods for incompressible viscous flow, Handbook of Numerical Analysis, Vol. IX, Ciarlet, P. G. and Lions, J. L. (eds.), North-Holland, Amsterdam, 2003, 3–1176.

[27] Girault, V. and Glowinski, R., Error analysis of a fictitious domain method applied to a Dirichlet problem, *Japan J. Indust. Appl. Math.*, **12**, 1995, 487–514.

[28] Chorin, A. J., Hughes, T. J. R., McCracken, M. F. and Marsden, J. E., Product formulas and numerical algorithms, *Comm. Pure Appl. Math.*, **31**, 1978, 205–256.

[29] Dean, E. J. and Glowinski, R., A wave equation approach to the numerical solution of the Navier-Stokes equations for incompressible viscous flow, *C. R. Acad. Sc. Paris, Série* 1, **325**, 1997, 783–791.

[30] Dean, E. J., Glowinski, R. and Pan, T. W., A wave equation approach to the numerical simulation of incompressible viscous fluid flow modeled by the Navier-Stokes equations, Mathematical and Numerical Aspects of Wave Propagation, De Santo, J. A. (ed.), SIAM, Philadelphia, 1998, 65–74.

[31] Alexeev, A., Verberg, R. and Balazs, A. C., Modeling the interactions between deformable capsules rolling on a compliant surface, *Soft Matter*, **2**, 2006, 499–509.

[32] Fischer, T. M., Stöhr-Liesen, M. and Schmid-Schönbein, H., The red cell as a fluid droplet: Tank tread-like motion of the human erythrocyte membrane in shear flow, *Science*, **202**, 1978, 894–896.

[33] Keller, S. R. and Skalak, R., Motion of a tank-treading ellipsoidal particle in a shear flow, *J. Fluid Mech.*, **120**, 1982, 27–47.

[34] Beaucourt, J., Rioual, F., Séon, T., et al., Steady to unsteady dynamics of a vesicle in a flow, *Phys. Rev. E*, **9**, 2004, 011906.

[35] Li, H. B., Yi, H. H., Shan, X. W. and Fang, H. P., Shape changes and motion of a vesicle in a fluid using a lattice Boltzmann model, *Europhysics Letters*, **81**, 2008, 54002.

[36] Lai, M.-C., Hu, W. F. and Lin, W. W., A fractional step immersed boundary method for stokes flow with an inextensible interface enclosing a solid particle, *SIAM. J. Sci. Comput.*, **34**, 2012, 692–710.

[37] Segré, G. and Silberberg, A., Radial particle displacements in Poiseuille flow of suspensions, *Nature*, **189**, 1961, 209–210.